

## High-order solitons and the modulational instability

Masataka Nakazawa, Kazunori Suzuki, and Hirokazu Kubota

*Transmission Systems Laboratories, Optical Communication Laboratory, Nippon Telegraph and Telephone Corporation, Tokai, Ibaraki-ken 319-11, Japan*

Hermann A. Haus

*Electrical Engineering and Computer Science and Research Laboratory of Electronics, Massachusetts Institute of Technology, Cambridge, Massachusetts 02319*

(Received 19 December 1988)

The connection between the modulational instability (MI) and the evolution of a higher-order soliton is described. The amplitude ripples that appear on the higher-order soliton can be regarded as a MI. A perturbation theory for higher-order solitons is developed to show differences between the cw MI and the pulsed MI. Initiation of the MI ripples on the soliton pulse is produced by MI amplification of the Fourier components of maximum gain. This phenomenon is corroborated by the study of the breakup of super-Gaussian pulses. Higher-order effects such as the third-order dispersion, shock, and the self-induced Raman effect in a nonlinear Schrödinger equation (NLS) are studied from the point of view of the MI process. It is shown that the Raman effect can enhance generation of the ripple because the parametric noise can build up faster than by MI alone as described by the NLS without perturbations.

### I. INTRODUCTION

The modulational instability (MI) in optical fibers is of great interest for the generation of pulse trains with a THz repetition rate.<sup>1</sup> We recently succeeded in achieving a modulation instability laser (MIL).<sup>2</sup> The MIL is pumped by mode-locked pulses of which the wavelength is in the negative group-velocity dispersion (GVD) regime (negative GVD).

Since the pump pulse is of relatively high peak intensity, the pump-pulse area corresponds to a very-high-order soliton. When the pump pulse is represented by a secant hyperbolic of area  $N$  times ( $N$  integer) the area of a fundamental soliton, the time evolution of this high-order soliton must be describable as a MI, at least before large-signal set in. The MI consists of three waves.<sup>1</sup> One is the pump wave, which is much larger than the Stokes wave (the second wave) and the anti-Stokes (the third wave). The theory of MI is only valid under the condition that the Stokes and the anti-Stokes amplitudes are much smaller than that of the pump.

In the present paper, we study numerically and analytically how the nonlinear Schrödinger equation (NLS) predicts the growth of the amplitude ripples in one pass along the fiber. With an excitation by a high-order soliton ( $N=40-300$ ), it is shown that the ripples on the pump soliton can be well explained with MI for a certain propagation distance and pump power. A perturbation theory for higher-order solitons is developed and differences between the higher-order solitons and the MI are discussed. In the next step, we show how the ripples grow up from the initial pump pulse. It is important to know how the ripples can be initiated without the input Stokes component. To investigate this, a super-Gaussian pulse ( $m=2$ ) is utilized in the computation because it has

a flat top and fall offs on both wings of the pulse. It is shown in Sec. V that there is no ripple generation initially on the flat top because the self-phase-modulation excitation is much smaller. Higher-order effects on the soliton such as third-order dispersion, shock, and the self-induced Raman effect are described in Sec. VI.

### II. EXCITATION OF HIGH-ORDER SOLITONS

We described experiments on the MIL pumped by mode-locked pulses from a color-center laser, the wavelength of which was set in the negative dispersion regime.<sup>2</sup> The pump power of 20–40 W for the MIL is much larger than the  $N=1$  soliton power of 10–20 mW, corresponding to a pulse width of 13 ps and a GVD of 1 ps/km nm. It can be expected that the MIL on the pump pulse is equivalent to the initial evolution of a very-high-order soliton.

The nonlinear Schrödinger equation is

$$(-i)\frac{\partial u}{\partial \xi} = \frac{1}{2}\frac{\partial^2 u}{\partial \tau^2} + |u|^2 u, \quad (1)$$

where the first term on the rhs (right-hand side) of Eq. (1) is due to GVD and the second term is due to the self-phase-modulation (SPM). The solution of the lowest-order soliton ( $N=1$  soliton) is

$$u(\xi, \tau) = 2\eta \operatorname{sech}(2\eta\tau) e^{i2\eta^2\xi}. \quad (2)$$

The initial value problem has been solved by Satsuma and Yajima,<sup>3</sup> and it has been shown that  $N$  soliton exists which satisfies

$$A + \frac{1}{2} > N \quad (3)$$

for an input pulse  $u(0, \tau) = A \operatorname{sech}(\tau)$ . Here,  $\eta$  is set

equal to  $\frac{1}{2}$  as a standard soliton. The  $N$ th-order soliton power  $P_N$  is related to the  $N=1$  soliton power  $P_{N=1}$

$$P_N = N^2 P_{N=1} \tag{4}$$

Figures 1(a)–1(c), corresponding to  $N=55, 58,$  and  $61,$  respectively, show the computed evolutions of higher-order solitons for different  $N$  numbers. The fiber length is fixed at 330 m. The nonlinear index  $n_2$  of the fiber was taken to  $3.2 \times 10^{-20} \text{ m}^2/\text{W}$ . In Fig. 1, upper, center, and lower traces show field amplitude  $E,$  chirp, and phase change with time. A dashed curve shows the input pulse waveform. To fit our experimental results, the full width at half maximum (FWHM) of the input sech pulse  $\tau_{\text{FWHM}},$  of 13 ps, and GVD of 1 ps/km nm were utilized. It is seen in Fig. 1 that the wings of the field waveform become steeper as it propagates down the fiber, and the chirp in the wings is rather smooth. With  $N=58,$  small ripples appear on the top of the output pulse, resulting in small changes in the chirped spectrum. With an increase of the pump power to  $N=61,$  we can clearly observe ripples like those of the MI and the chirp and the phase change accordingly.

The ripples are generated through the following process. When the self-phase modulation results in a chirp, the leading part of the pulse has a lower frequency and moves more slowly than the lagging part of the pulse at a

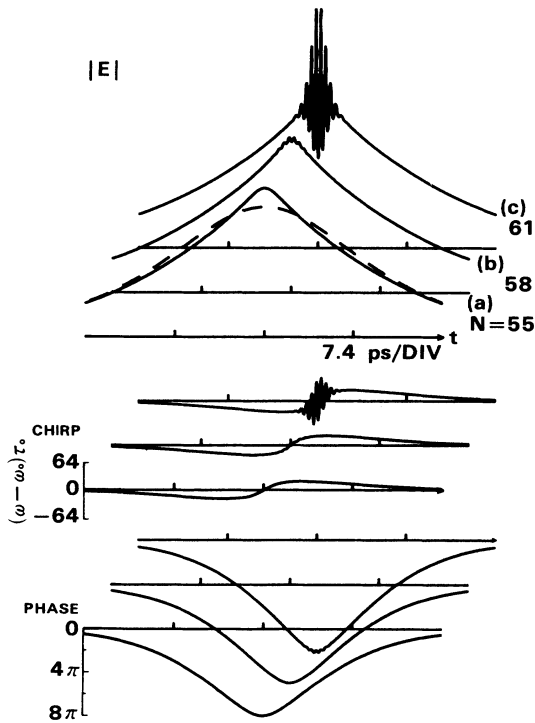


FIG. 1. Waveform changes of the higher-order solitons for different  $N$  number at  $l=330$  m. Traces (a), (b), and (c) correspond to  $N=55, 58,$  and  $61.$  Upper, center, and lower traces show field amplitudes  $|E|,$  chirps, and phase changes with time in each  $N$  number, respectively. Dashed curve shows the input pulse waveform.

higher frequency. The two components meet at the center and produce a ripple. This ripple grows most rapidly for the synchronous Stokes and anti-Stokes frequency components.

The soliton period  $Z_{\text{sp}}$  is related to the normalized distance  $Z_0$  via

$$Z_{\text{sp}} = \frac{\pi}{2} Z_0 = 0.322 \left[ \frac{\pi^2 c}{\lambda^2} \right] \frac{\tau_{\text{FWHM}}^2}{|D|} \tag{5}$$

where  $\lambda$  is the wavelength,  $\tau_{\text{FWHM}}$  is the full width at half maximum of the input pulse, and  $D$  is GVD. Thus,  $Z_{\text{sp}}$  is calculated to be 67.1 km. Therefore, a typical fiber length for a MIL is much shorter than  $Z_{\text{sp}}.$  For example, the fiber length of 330 m corresponds to  $4.9 \times 10^{-3} Z_{\text{sp}}.$

Figures 2(a)–2(c) correspond to spectra for Figs. 1(a)–1(c), respectively. In Figs. 2(a) and 2(b), although the spectrum of the pump soliton pulse is broadened through SPM, no significant sideband signal appears in the spectrum. In Fig. 2(c), there appear small sidebands and the spectral width of the pump pulse is further broadened. The vertical axis of the figure is 100 times expanded in Fig. 2(d), where two sidebands are clearly seen.

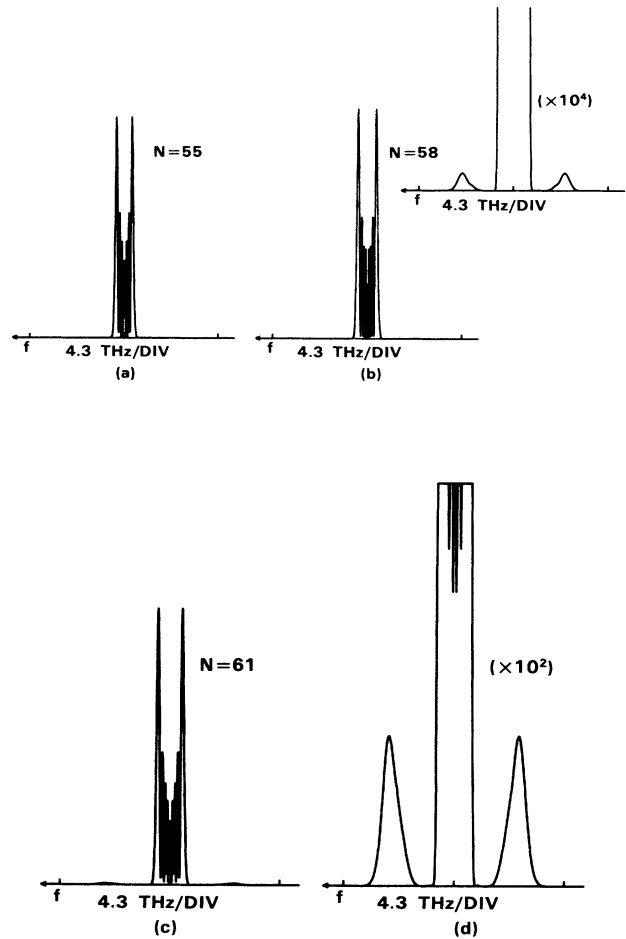


FIG. 2. Spectra for Figs. 1(a)–1(c). The vertical axis of (c) is 100 times expanded in (d).

In the next step, we show how the ripples grow along the fiber under a fixed pump power of  $N=61$ . Figures 3(a)–3(c) correspond to soliton waveforms at fiber lengths of 270, 300, and 330 m. Spectra for Figs. 3(a) and 3(b) are shown in Figs. 4(a) and 4(b). From Figs. 3 and 4, it is seen that ripples gradually build up along the fiber entirely due to the spectral components of the high-order soliton without an addition of any noise components. From the sideband spectral amplitude at  $l=330$  m in Fig. 2(d) and that at  $l=300$  m in Fig. 4(b), the amplitude gain of the ripple is numerically estimated to be about  $g=0.1 \text{ m}^{-1}$ . When one attributes this to the MI process, the amplitude gain of the MI is given by<sup>1,2</sup>

$$g_{\max} = \frac{\omega}{c} n_2 \frac{N^2 P_{N=1}}{\pi W_0^2}, \quad (6)$$

where  $W_0$  is mode size and  $P_{N=1}$  is the  $N=1$  soliton power given by<sup>4</sup>

$$P_{N=1} = 0.776 \frac{\lambda^3}{\pi^2 c n_2} \frac{|D|}{\tau_{\text{FWHM}}^2} \pi W_0^2. \quad (7)$$

Here the  $P_{N=1}$  is calculated to be 14 mW and therefore  $N^2 P_{N=1}$  is 52.1 W. For  $W_0=5 \mu\text{m}$ ,  $g_{\max}$  is calculated as  $0.09 \text{ m}^{-1}$  and is in good agreement with the above value.

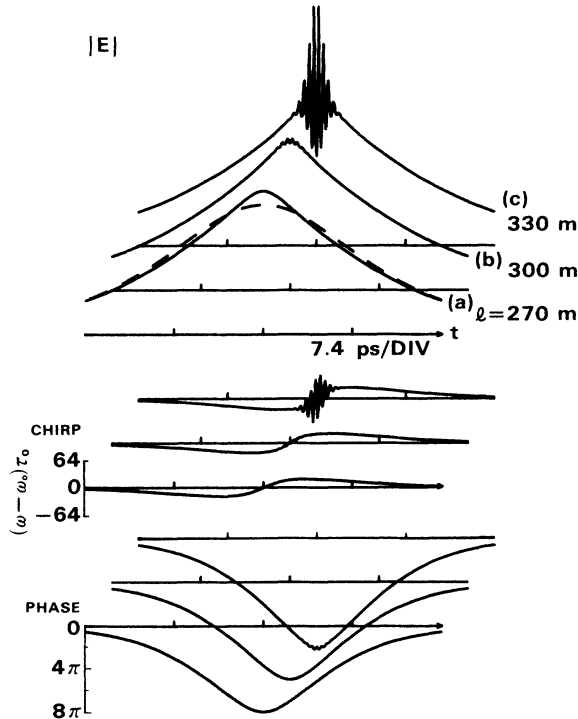


FIG. 3. Waveform changes for the higher-order solitons at different fiber lengths. (a), (b), and (c) correspond to fiber lengths of 270, and 300, and 330 m, respectively.  $N$  is kept at 61. Upper, center, and lower traces show field amplitudes  $E$ , chirps, and phase changes with time for each fiber length, respectively. Dashed curve shows the input pulse waveform.

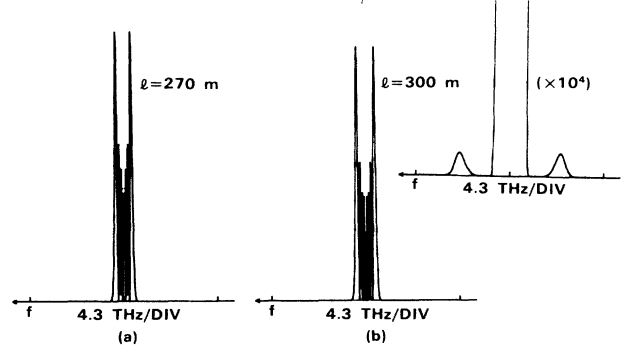


FIG. 4. Spectra for Figs. 3(a) and 3(b).

### III. MODULATIONAL INSTABILITY AND HIGHER-ORDER SOLITONS

In this section, we investigate how the ripples on the higher-order solitons are related to MI. The modulation frequency  $f_{\text{MI}}$  in the MI process is given by<sup>1,2</sup>

$$f_{\text{MI}} = \frac{1}{2\pi} \left[ \frac{\omega}{c} \left| \frac{n_2}{k''} \frac{N^2 P_{N=1}}{\pi W_0^2} \right| \right]^{1/2}. \quad (8)$$

The ripple frequencies on the higher-order solitons and the theoretical fit of MI are shown in Figs. 5(a) and 5(b) as functions of  $|D|$ . The solid lines are theoretical  $f_{\text{MI}}$  from Eq. (8). Here  $N$  is set at  $N=55$  with  $|D|=1 \text{ ps/km nm}$ , corresponding to a pump power of 42.9 W in Fig. 5(a) for  $\tau_{\text{FWHM}}$  of 13 ps and  $W_0$  of  $5 \mu\text{m}$ . Open and closed circles refer to fiber lengths of 300 and 350 m, where it is clearly seen that those results agree well with the MI frequency  $f_{\text{MI}}$ . Strictly speaking, there is a difference between  $f_{\text{ripple}}$  and  $f_{\text{MI}}$  in that the ripple frequency changes along the fiber, while  $f_{\text{MI}}$  is fixed. At shorter fiber lengths, the  $f_{\text{ripple}}$  is close to  $f_{\text{MI}}$ . These features are discussed theoretically in Sec. IV. It is also seen that the ripple frequency starts to deviate from the MI frequency around  $|D|=1 \text{ ps/km nm}$ .

These results demonstrate a relationship between the ripple duration and  $\tau_{\text{FWHM}}$ . The following condition is required, in order that the ripples be interpretable in terms of MI:

$$f_{\text{ripple}} \ll 1/\tau_{\text{FWHM}}. \quad (9)$$

Then, one has

$$f_{\text{MI}} = f_{\text{ripple}} \quad \text{for } l \ll Z_{\text{sp}}. \quad (10)$$

Closer agreement between  $f_{\text{ripple}}$  and  $f_{\text{MI}}$  is obtained in Fig. 5(b) when  $N$  is set at 70 at  $|D|=1 \text{ ps/km nm}$  corresponding to  $P_N=67.4 \text{ W}$  and the fiber length is 223 m. The fiber length is shorter than those in Fig. 5(a).

Figure 6(a) shows the dependence of  $f_{\text{ripple}}$  on soliton number  $N$ , where  $\bullet$ ,  $\circ$ ,  $\triangle$ , and  $\square$  correspond to fiber lengths of 200, 300, 330, and 360 m, respectively. The very-high-order soliton case at shorter propagation distances is given in Fig. 6(b). Theoretical curves for  $f_{\text{MI}}$

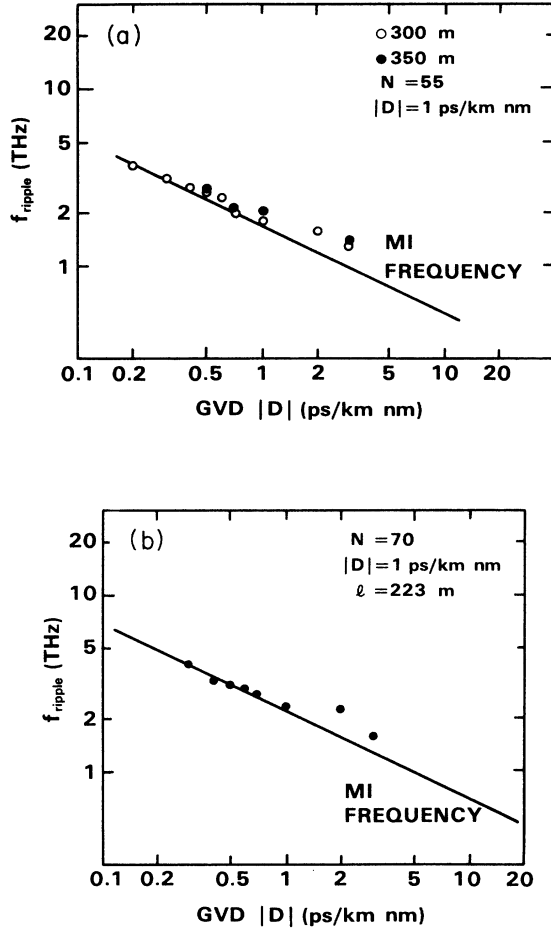


FIG. 5. Relationship between  $f_{\text{ripple}}$  on the higher-order solitons and the theoretical MI frequency as a function of  $|D|$ . For 5(a),  $N$  is kept at 55, with  $|D| = 1$  ps/km nm. Open and closed circles refer to fiber lengths of 300 and 350 m. For (b),  $N$  is 70 at  $|D| = 1$  ps/km nm and the fiber length is 223 m.

are also given in the figures. It is clearly seen that  $f_{\text{ripple}}$  depends on fiber length and it becomes closer to  $f_{\text{MI}}$  when the fiber length is short and  $N$  is large. In other words,  $f_{\text{ripple}}$  is a function of fiber length for a fixed  $N$ , which is quite reasonable because interaction forces among the  $N=1$  solitons forming out of this ripple changes along the fiber. Although there are weak second sidebands at different frequencies, they were neglected. In the region  $1 \ll Z_{\text{sp}}$ ,  $f_{\text{ripple}}$  increases with increasing length of the fiber.

For comparison consider the case of infinite  $\tau_{\text{FWHM}}$ , i.e., the cw case, which corresponds to a pure MI condition. Then, the  $N=1$  soliton goes to zero and, therefore,  $N$  becomes infinite for a fixed pump power.  $Z_{\text{sp}}$  also goes to infinity. These conditions can be approximated by higher-order solitons of very large  $N$  and by evaluating  $f_{\text{ripple}}$  at relatively short fiber lengths. This result is shown in Fig. 6(b), in which  $f_{\text{ripple}}$  agrees well with the theoretical  $f_{\text{MI}}$ .

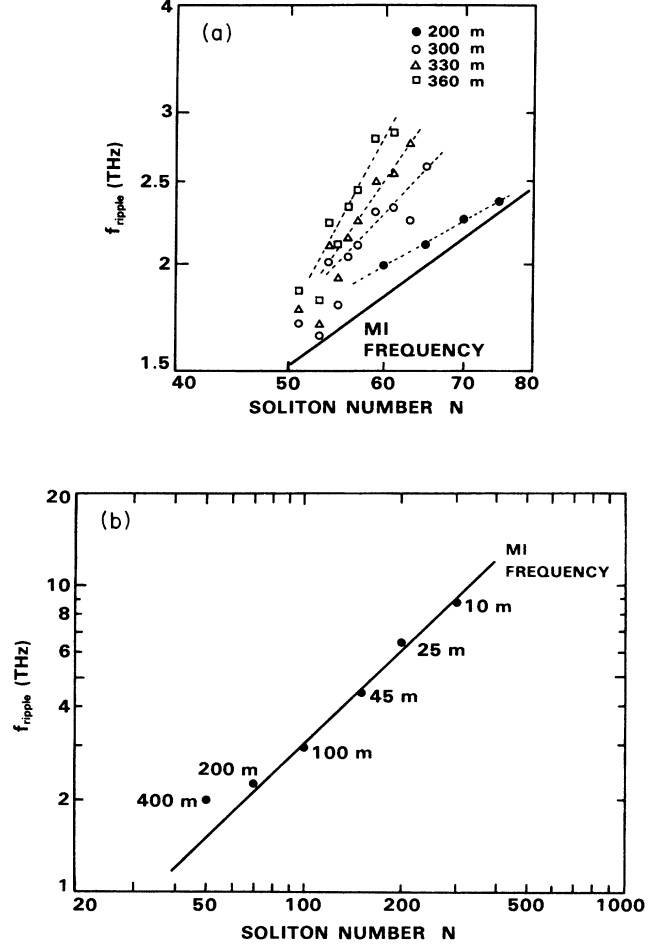


FIG. 6. Dependence of  $f_{\text{ripple}}$  on soliton number  $N$ . In (a),  $\bullet$ ,  $\circ$ ,  $\triangle$ , and  $\square$  correspond to fiber lengths of 200, 300, 330, and 360 m, respectively. In (b),  $f_{\text{ripple}}$  for higher  $N$  numbers (50–300) at shorter fiber lengths are given. Solid lines in (a) and (b) show theoretical  $f_{\text{MI}}$ .

#### IV. PERTURBATION THEORY ON HIGHER-ORDER SOLITONS

We develop here a perturbation theory of higher-order solitons and discuss how the excitation of the solitons relates to MI. A difference between the cw MI and the pulsed MI is also discussed.

Putting the soliton waveform  $u$  as

$$u = U(\xi, \tau) e^{if(\xi, \tau)} \quad (11)$$

and inserting into Eq. (1), one obtains the following two equations: From the real part,

$$U \frac{\partial f}{\partial \xi} = \frac{1}{2} \frac{\partial^2 U}{\partial \tau^2} - \frac{1}{2} U \left[ \frac{\partial f}{\partial \tau} \right]^2 + U^3 \quad (12)$$

and from the imaginary part

$$-\frac{\partial U}{\partial \xi} = \frac{1}{2} U \frac{\partial^2 f}{\partial \tau^2} + \frac{\partial f}{\partial \tau} \frac{\partial U}{\partial \tau} \quad (13)$$

By expanding  $U$  as a power of  $\xi$ ,  $U(\xi, \tau)$  is written as

$$U(\xi, \tau) = \sum_{n=0}^{\infty} \hat{U}_n(\tau) \xi^n \\ = \hat{U}_0(\tau) + \hat{U}_1(\tau) \xi + \hat{U}_2(\tau) \xi^2 + \dots \quad (14)$$

Noting that derivatives of  $U$  and  $f$  with respect to  $\tau$  in higher-order solitons are smaller than those in lower-order solitons, we neglect the first two terms on the rhs of Eq. (12) and approximate the equation by

$$\frac{\partial f}{\partial \xi} \cong U^2 \quad (15)$$

thus,

$$f(\xi, \tau) = \int_0^{\xi} U^2(\xi', \tau) d\xi' \\ = \hat{U}_0^2 \xi + \hat{U}_0 \hat{U}_1 \xi^2 + \frac{1}{3} (\hat{U}_1 + 2\hat{U}_0 \hat{U}_2) \xi^3 \\ + \frac{1}{2} (\hat{U}_1 \hat{U}_2 + \hat{U}_0 \hat{U}_3) \xi^4 \\ + \frac{1}{5} (\hat{U}_2^2 + 2\hat{U}_0 \hat{U}_4 + 2\hat{U}_1 \hat{U}_3) \xi^5 + \dots \quad (16)$$

Putting Eqs. (14) and (16) into Eq. (13), we obtain the following relationship for each coefficient of  $\xi^n$  ( $n=0, 1, 2, \dots$ ):

$$\hat{U}_1 = 0 \quad \text{for } \xi^0, \quad (17a)$$

$$\hat{U}_2 = -\frac{1}{2} [\hat{U}_0' (\hat{U}_0^2)' + \frac{1}{2} \hat{U}_0 \hat{U}_0'''] \quad \text{for } \xi^1, \quad (17b)$$

$$\hat{U}_3 = 0 \quad \text{for } \xi^2, \quad (17c)$$

$$\hat{U}_4 = \frac{1}{4} [\frac{2}{3} \hat{U}_0' (\hat{U}_0 \hat{U}_2)' + \hat{U}_2' (\hat{U}_2^2)' + \frac{1}{3} \hat{U}_0 (\hat{U}_0 \hat{U}_2)'' \\ + \frac{1}{2} \hat{U}_2 (\hat{U}_2^2)'''] \quad \text{for } \xi^3. \quad (17d)$$

It is obvious that  $\hat{U}_n$  for  $n$  odd is always zero because amplitude effects are even, phase effects are odd, in an expression in terms of  $\xi$ .

With

$$\hat{U}_0(\tau) = N \operatorname{sech}(\tau), \quad (18)$$

we have

$$\hat{U}_2(\tau) = N^3 \operatorname{sech}^3(\tau) [-2 \tanh^2(\tau) + \frac{1}{2} \operatorname{sech}^2(\tau)], \quad (19)$$

$$\hat{U}_4(\tau) = N^5 \operatorname{sech}^5(\tau) [\frac{17}{24} - \frac{145}{12} \tanh^2(\tau) + \frac{155}{8} \tanh^4(\tau)]. \quad (20)$$

Setting  $\tau=0$ , we can estimate how the peak amplitude changes along the fiber. Hence

$$U(\xi, \tau=0) = N + \frac{1}{2} N^3 \xi^2 + \frac{17}{24} N^5 \xi^4 + \dots \quad (21)$$

For the phase factor  $f(\xi, \tau)$

$$f(\xi, \tau) = \hat{U}_0^2 \xi + \frac{2}{3} \hat{U}_0 \hat{U}_2 \xi^3 + \frac{1}{5} (\hat{U}_2^2 + 2\hat{U}_0 \hat{U}_4) \xi^5 + \dots \quad (22)$$

Similarly,  $f(\xi, \tau=0)$  is given by

$$f(\xi, \tau) = N^2 \xi + \frac{1}{3} N^4 \xi^3 + \frac{1}{3} N^6 \xi^5 + \dots \quad (23)$$

The amplitude change  $U(\xi, \tau=0)$  and phase change

$f(\xi, \tau=0)$  thus obtained are shown in Figs. 7 and 8, respectively, where the  $N$  numbers are 50, 70, 100, and 200. The solid lines show the exact evolution of  $U(\xi, \tau=0)$  and  $f(\xi, \tau=0)$  calculated by NLS. Dotted lines are due to the perturbation theory and dash-dotted lines are the case when  $\partial f / \partial \xi = U^2$  and  $\partial U / \partial \xi = 0$ , resulting in  $U(\xi) = \text{const}$  and  $f = U^2 \xi$ . According to these figures, the present perturbation agrees well with the direct calculation from the NLS. Higher  $N$  numbers lead to closer agreement, as expected. The amplitude and the phase change moderately at an early stage of the soliton propagation. However, the solitons start to have rapid changes at a certain distance, at which the coherent MI process disappears. We conclude that MIL can be achieved when the change of  $U(\xi, \tau)$  as a function of  $\xi$  is small and  $f(\xi, \tau)$  follows approximately  $U^2 \xi$ .

When the second and the third terms of Eq. (21) are smaller than  $N$ , one may put Eq. (21) into Eq. (8). Thus we obtain a modified MI frequency  $f_{\text{MI}}(\xi)$ , which varies along the fiber

$$f_{\text{MI}}(\xi) = (1 + \frac{1}{2} N^2 \xi^2) f_{\text{MI}}. \quad (24)$$

This means that  $f_{\text{MI}}(\xi)$  increases by a factor of  $1 + \frac{1}{2} N^2 \xi^2$  as a function of distance. Figure 6(a) can be explained by the present results. Let us consider how the MI gain changes along the fiber. From Eqs. (6) and (8), we have

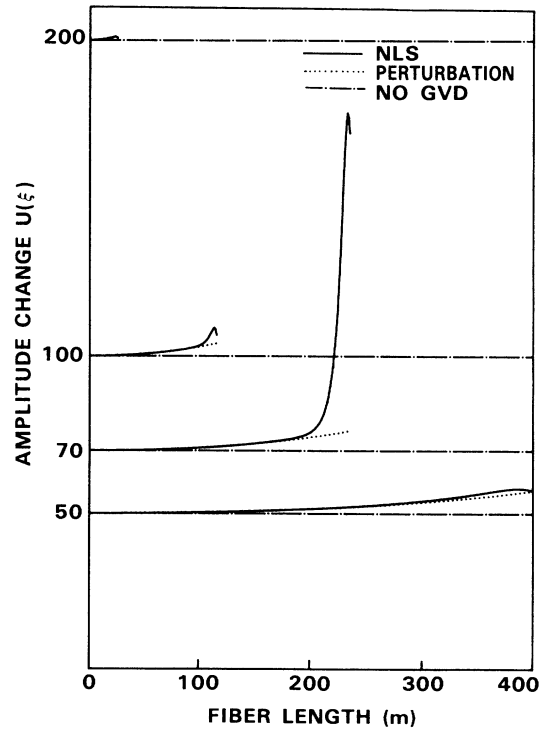


FIG. 7. Amplitude changes of the higher-order solitons as a function of  $\xi$ .  $N$  numbers are 50, 70, 100, and 200. The solid, dotted, and dash-dotted lines show the exact calculation of NLS, the perturbation theory, and the case of no group-velocity dispersion, respectively.

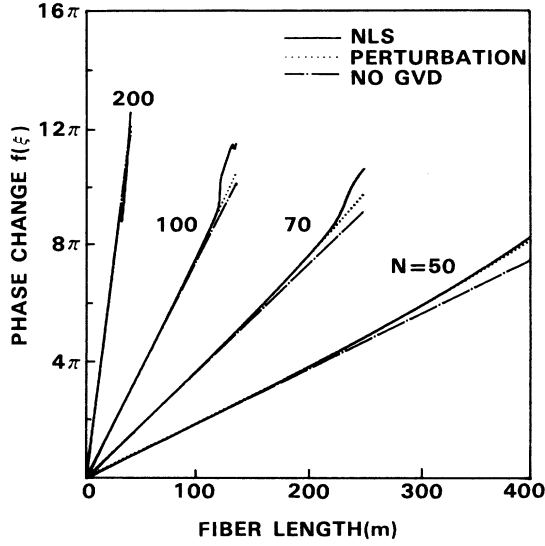


FIG. 8. Phase changes of the higher-order solitons as a function of  $\xi$ . The conditions are the same as in Fig. 7.

$$g_{\max} = |k''| \Omega_{\text{MI}}^2. \quad (25)$$

Putting Eq. (24) into Eq. (26),  $g_{\max}(\xi)$  can be given as

$$\begin{aligned} g_{\max}(\xi) &= (1 + \frac{1}{2} N^2 \xi^2)^2 |k''| \Omega_{\text{MI}}^2 \\ &= (1 + N^2 \xi^2) g_{\max}, \end{aligned} \quad (26)$$

and hence a total gain  $G_{\max}$  is given by

$$\begin{aligned} G_{\max} &= \int_0^{\xi} g_{\max}(\xi') d\xi' \\ &= (1 + \frac{1}{3} N^2 \xi^2) (g_{\max} \xi). \end{aligned} \quad (27)$$

There are many combinations between  $N$  and  $\xi$  to keep the gain constant in Eq. (27)

$$N^2 \xi (1 + \frac{1}{3} N^2 \xi^2) = C, \quad (28)$$

where  $C$  is constant. Thus  $N^2 \xi^2$  can be approximated as

$$\begin{aligned} N^2 \xi^2 &= -\frac{3}{2} + (\frac{9}{4} + \frac{3}{4} \xi C)^{1/2} \\ &\approx \frac{1}{4} \xi C. \end{aligned} \quad (29)$$

Putting Eq. (28) into Eq. (24), we have

$$f_{\text{MI}}(\xi) = (1 + \frac{1}{8} C \xi) f_{\text{MI}}. \quad (30)$$

Accordingly, when the MI gain is kept constant,  $f_{\text{MI}}(\xi)$  linearly deviates from  $f_{\text{MI}}$ . This has been shown in Fig. 6(b), in which  $f_{\text{MI}}(\xi)$  for shorter length agrees well with theoretical  $f_{\text{MI}}$ . However,  $f_{\text{MI}}(\xi)$  deviates from  $f_{\text{MI}}$  when  $\xi$  is long.

In addition, we can speculate from Eq. (27) that a combination of smaller  $N$  and larger  $\xi$  gives larger MI gain than that of larger  $N$  and smaller  $\xi$  when  $N^2 \xi$ , which gives MI gain at cw pump wave, is kept constant. We have investigated two cases to verify this result. One is  $N=50$  and  $l=400$  m, and the other is  $N=300$  and  $l=12$  m. They are shown in Figs. 9(a) and 9(b), respectively. It

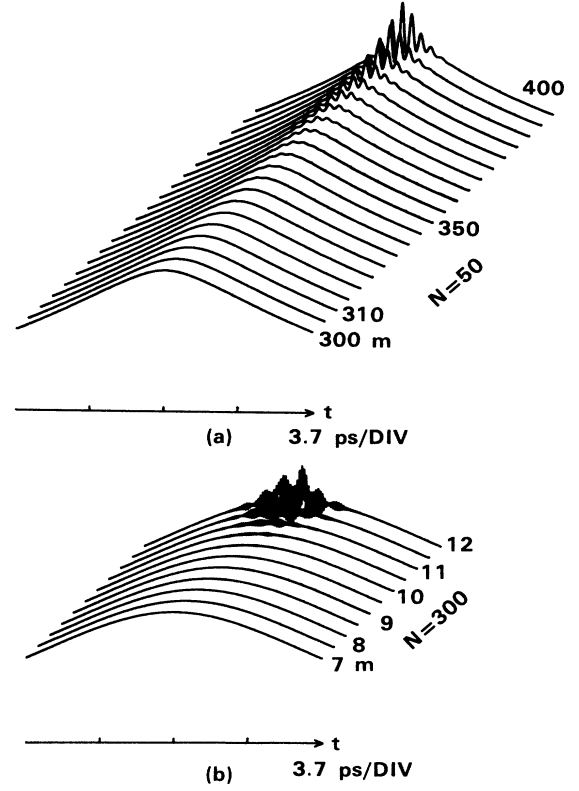


FIG. 9. Comparison of the buildup distances of the MI for  $N=50$  and the  $N=300$  solitons. (a)  $N=50$ ; (b)  $N=300$ .

is seen that both pulses have MI ripples. To investigate detailed growth of the ripples, Fourier spectral changes of the Stokes waves corresponding to Figs. 9(a) and 9(b) are given in Figs. 10(a) and 10(b), respectively. Here, we find that the gain of the case (a) builds up faster than the case (b). The buildup of the Stokes for  $N=300$  soliton starts at 12 m, which corresponds to  $l=432$  m for  $N=50$  soliton when keeping  $N^2 \xi$  constant. However, the Stokes builds up in shorter distance around 400 m. This result agrees with our prediction. The physical interpretation is that the amplitude change of the lower-order soliton is larger than that of the higher-order soliton, so that the MI gain for the lower  $N$  and longer  $\xi$  becomes larger.

## V. INITIATION OF THE MI RIPPLES IN HIGHER-ORDER SOLITONS

The MI under pulsed operation is initiated by the Fourier components of the pulse, so that the shape of the pump pulse plays an important role in generation of the modulation ripples. Figures 11(a)–11(c) show how the MI ripples grow when the pump pulse is a super-Gaussian ( $m=2$ ) which has a relatively flat plateau at the center of the pump pulse. Traces (a), (b), and (c) are for fiber lengths of 280, 320, and 350 m, respectively. The amplitude of the pulse is chosen to correspond to  $N=60$ . The dashed curve shows the original waveform, where  $\tau_{\text{FWHM}}$  is set to 14.8 ps. The initial envelope gradually changes in Fig. 11(a), and both sides get sharpened.

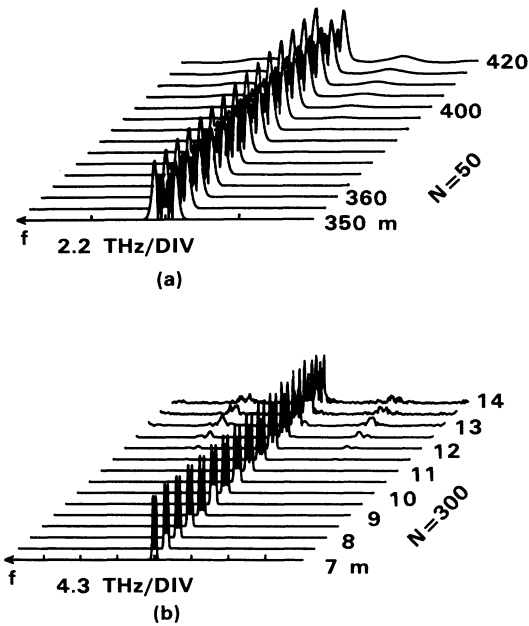


FIG. 10. Comparison of the Stokes spectra for  $N=50$  and  $N=300$  solitons along the fiber. (a)  $N=50$ , (b)  $N=300$ . MI for  $N=50$  builds up faster than that for  $N=300$  when  $N^2\xi$  is kept constant.

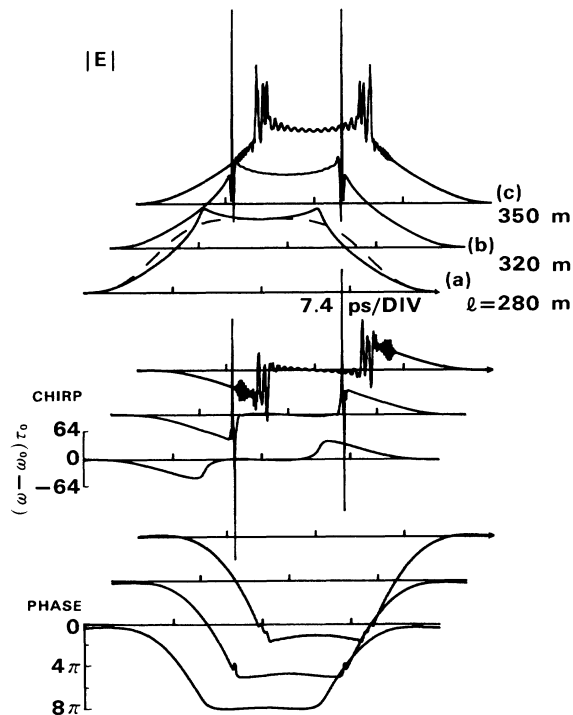


FIG. 11. MI ripple growth for a super-Gaussian input. The peak power corresponds to  $N=60$ . Traces (a), (b), and (c) refer to fiber lengths of 280, 320, and 350 m, respectively.

When the pump pulse propagates further, small ripples rapidly appear on the steeper parts of the envelope. Here it should be noted that no ripples are observed at the center of the pump because there exists no SPM at the center (the center is flat at first). With further propagation along the fiber as shown in (c), the modulation ripples build up over the entire pump pulse.

## VI. PERTURBATIONS ON MI RIPPLES IN HIGHER-ORDER SOLITONS

To achieve pure MI ripples on a higher-order soliton, it is important to increase  $f_{\text{ripple}}$  by decreasing the GVD value, which results in decreasing the  $N=1$  soliton energy. This is equivalent to increasing the  $N$  number. When the soliton energies are small, they are likely to be disturbed by perturbations such as third-order dispersion  $k'''$ , shock-term, and the self-induced Raman effect.<sup>5</sup> When these perturbations are incorporated in NLS, Eq. (1) is modified as

$$\begin{aligned}
 (-i) \frac{\partial u}{\partial \xi} - \frac{1}{2} \frac{\partial^2 u}{\partial \tau^2} - |u|^2 u \\
 = -i \frac{k'''}{6|k''|\tau_0} \frac{\partial^3 u}{\partial \tau^3} + i \frac{2}{\omega_0 \tau_0} \frac{\partial}{\partial \tau} (|u|^2 u) \\
 - \frac{\tau_n}{\tau_0} u \frac{\partial}{\partial \tau} |u|^2, \quad (31)
 \end{aligned}$$

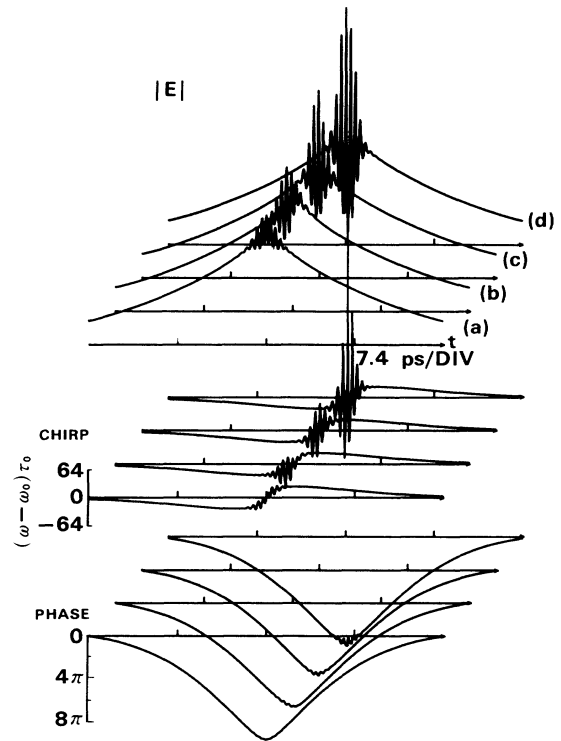


FIG. 12. MI ripple growths for perturbed higher-order solitons. Traces (a), (b), (c), and (d) correspond to the cases without perturbation, with  $k'''$  ( $k'''/6|k''|\tau_0=1.5 \times 10^{-3}$ ), with shock term ( $2/\omega_0\tau_0=2.2 \times 10^{-4}$ ), and with self-induced Raman effect ( $\tau_n/\tau_0=8 \times 10^{-4}$ ), respectively.

where  $\omega_0$  is angular carrier frequency of the pulse  $\tau_0 = (|k''|/z_0)^{1/2} (= \tau_{\text{FWHM}})$  which satisfies  $\tau = t/\tau_0$  and  $\xi = z/z_0$ , and  $\tau_n$  is a relaxation time of the nonlinear index which satisfies

$$\frac{\partial \Delta n(t)}{\partial t} = \frac{\Delta n(t)}{\tau_n} + \frac{n_2}{\tau_n} |E(t)|^2. \quad (32)$$

In our experiments,  $D (= 2\pi c k''/\lambda^2)$  is  $-1$  ps/km nm and

$$\frac{\partial D}{\partial \lambda} \left[ = -\frac{2}{\lambda} D - \left( \frac{2\pi c}{\lambda^2} \right)^2 k''' \right]$$

is  $-0.052$  ps/km nm<sup>2</sup>. Then we have  $k'' = -1.3 \times 10^{-27}$  s<sup>2</sup>/m,  $k''' = 8.7 \times 10^{-41}$  s<sup>3</sup>/m, and  $\tau_0 = 7.4$  ps ( $\tau_{\text{FWHM}} = 13$  ps). Thus  $k'''/6|k''|\tau_0$  is  $1.5 \times 10^{-3}$ . For the shock term,  $2/\omega_0\tau_0$  is  $2.2 \times 10^{-4}$  for  $\tau_0 = 7.4$  ps and  $\lambda = 1.55$   $\mu\text{m}$ . The Raman term  $\tau_n/\tau_0$  is  $8 \times 10^{-4}$  by using  $\tau_n$  of 5.3 fs.<sup>6</sup>

Figure 12(a) shows MI-like ripples when no perturbations are applied, where  $N=60$  and  $l=340$  m. At the top of the waveform, clear ripples are observed. With an addition of  $k'''$ , the waveform with the same  $N$  and  $l$  changes to that of Fig. 12(b), in which the ripple becomes four times as large, and asymmetry is also observed. When the shock term is added [Fig. 12(c)], the waveform has changes similarly, where the asymmetry is smaller than that in Fig. 12(b) although the ripple amplitude is larger. When the Raman term is added [Fig. 12(d)], the ripples are considerably amplified [seven times larger than that in (a)]. These results mean that one of the most effective perturbation terms for the ripple generation is the Raman term. As pointed out by Tai *et al.*,<sup>7</sup> the Raman term is the most crucial for soliton fission. This has also been proven from the present results.

It is also found from Fig. 12 that the MI-like ripples are enhanced when the perturbations are added. This is due to the fact that zero crossing point of the nonlinear frequency shift is moved to the slope of the soliton pulse, while it occurs at the center of the pulse when no perturbation is applied. Accordingly, the amplitude modulation due to an optical wave breaking<sup>8</sup> is strongly enhanced because the phase changes rapidly with time when the zero frequency shift occurs on the slope of the pulse. Hence, the Stokes and anti-Stokes build up faster than in the case of no perturbation.

The spectral changes corresponding to Figs. 12(a)–12(d) are shown in Figs. 13(a)–13(d). A small asymmetry between the Stokes and the anti-Stokes spectra is observed in (b) and (c). In the case of the Raman effect shown in (d), the asymmetry between the Stokes and the anti-Stokes amplitudes is further enhanced and the Stokes signal builds up strongly. For the self-induced Raman effect, caused by a noninstantaneous response of the nonlinear index, the Stokes amplitude is amplified

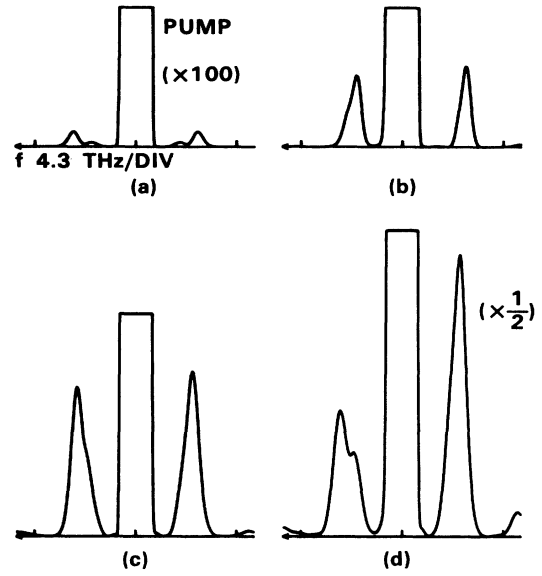


FIG. 13. Frequency spectra of Figs. 12(a)–12(d). Vertical axis of (a) is 100 times extended and that of (c) is  $\frac{1}{2}$  reduced for convenience.

and the anti-Stokes amplitude is absorbed. Nevertheless, the anti-Stokes component is amplified somewhat in (d) compared with (a). Because it is amplified through the MI process and absorbed by the Raman effect.

## VII. CONCLUSION

It has been shown that the amplitude ripple which appears on a higher-order soliton can be regarded as a MI process, provided that the ripple duration is much shorter than the pulse duration of the pump. The ripple frequency generated in a higher-order soliton at shorter propagation distances agree well with the MI frequency. This has also been proven by a simple perturbation theory. The initiation of the MI ripple on the pump is achieved by spectral components of the pulse and do not require any spontaneous emission. It has been shown that the self-induced Raman effect can enhance the growth rate of the MI ripples, because an asymmetric amplitude change occurs on the wing of the pump pulse and resultant phase change initiates the MI ripple.

## ACKNOWLEDGMENTS

The authors would like to express their thanks to F. Ashiya and H. Kimura for their encouragements. This work (H.A.H.) was supported in part by the National Science Foundation Grant No. 8700474-EET.

<sup>1</sup>A. Hasegawa and W. F. Brinkman, IEEE J. Quantum Electron. QE-16, 694 (1980); see also, K. Tai, A. Hasegawa, and A. Tomita, Phys. Rev. Lett. 56, 135 (1986).

<sup>2</sup>M. Nakazawa, K. Suzuki, and H. A. Haus, IEEE J. Quantum

Electron. (to be published); see also, M. Nakazawa, K. Suzuki, and H. A. Haus, Phys. Rev. A 38, 5193 (1988).

<sup>3</sup>J. Satsuma and N. Yajima, Suppl. Prog. Theor. Phys. 55, 284 (1974).

<sup>4</sup>L. F. Mollenauer and R. H. Stolen, *Opt. Lett.* **9**, 13 (1985).

<sup>5</sup>J. P. Gordon, *Opt. Lett.* **11**, 662 (1986).

<sup>6</sup>H. A. Haus and M. Nakazawa, *J. Opt. Soc. Am. B* **4**, 652 (1987).

<sup>7</sup>K. Tai, A. Hasegawa, and N. Bekki, *Opt. Lett.* **13**, 392 (1988).

<sup>8</sup>W. J. Tomlinson, R. H. Stolen, and A. M. Johnson, *Opt. Lett.* **10**, 457 (1985).